ORIGINAL ARTICLE

Establishing a process route for additive manufacturing of NiCu-based Alloy 400: an alignment of gas atomization, laser powder bed fusion, and design of experiments

Jan-Philipp Roth[1] · Ivo Šulák[2] · Tomáš Kruml[2] · Wojciech Polkowski[3] · Tomasz Dudziak[3] · Peter Böhlke[4] · Ulrich Krupp[5] · Katrin Jahns[1]

Abstract

Alloy 400 is a corrosion-resistant, NiCu-based material which is used in numerous industrial applications, especially in marine environments and the high-temperature chemical industry. As conventional manufacturing limits geometrical complexity, additive manufacturing (AM) of the present alloy system promises great potential. For this purpose, a robust process chain, consisting of powder production via gas atomization and a design of experiment (DoE) approach for laser powder bed fusion (LPBF), was developed. With a narrow particle size distribution, powders were found to be spherical, flowable, consistent in chemical composition, and, hence, generally applicable to the LPBF process. Copper segregations at grain boundaries were clearly detected in powders. For printed parts instead, low-intensity micro-segregations at cell walls were discovered, being correlated with the iterative thermal stress applied to solidified melt-pool-near grains during layer-by-layer manufacturing. For the production of nearly defect-free LPBF structures, DoE suggested a single optimum parameter set instead of a broad energy density range. The latter key figure was found to be misleading in terms of part densities, making it an outdated tool in modern, software-based process parameter optimization. On the microscale, printed parts showed an orientation of melt pools along the build direction with a slight crystallographic [101] texture. Micro-dendritic structures were detected on the nanoscale being intersected by a high number of dislocations. Checked against hot-extruded reference material, the LPBF variant performed better in terms of strength while lacking in ductility, being attributed to a finer grain structure and residual porosity, respectively.

1 Introduction

Alloy 400 is a NiCu-based alloy, consisting mainly of two-thirds nickel and one-third copper, respectively. Both, nickel and copper, crystallize in a face-centered cubic (fcc) structure and form a solid solution [1–3]. Thus, Alloy 400, also known as Monel 400, consists of one phase only and shows isomorphic characteristics [2, 4, 5]. Further alloying elements with marginal proportions are iron, silicon, manganese, aluminum, and carbon.

The alloy shows excellent corrosion resistance in various media, such as acids, bases, and sea water [1, 4, 6–8]. It finds its application in steam generator tubes as well as in gas- and liquid-carrying pipelines for power plants. In the field of shipbuilding and marine technology, impellers, pump shafts, and splash zone claddings on offshore

✉ Jan-Philipp Roth
  j.roth@hs-osnabrueck.de

1 Faculty of Engineering and Computer Science, Osnabrück University of Applied Sciences, 49076 Osnabrück, Germany

2 Institute of Physics of Materials, Czech Academy of Sciences, 61600 Brno, Czech Republic

3 Krakow Institute of Technology, Łukasiewicz Research Network, 30-418, Kraków, Poland

4 KME Germany GmbH, Klosterstraße 29, 49074 Osnabrück, Germany

5 Steel Institute IEHK, RWTH Aachen University, 52072 Aachen, Germany

platforms are made of Alloy 400. In pump construction, components are facing a combined stress resulting from abrasion, erosion, corrosion, and chemical resistance, which is why Alloy 400 can be considered indispensable within this field [9]. Generally speaking, products being manufactured out of Monel alloys are very long-lasting due to their long-term resistance to the environment [8]. Further benefits of Alloy 400 are its good ductility and easy cold formability, which opens up a wide variety of engineering systems [10]. It behaves ductile at temperatures below 0 °C, meaning that it does not show brittle properties in a cold state [5].

With nickel being the base material, the alloy has great potential in high-temperature environments as well [11]. Also, due to the high copper content within Alloy 400, heat exchangers for combustion engines can be considered a further area of application [12]. Most importantly, critical component failure due to metal dusting, as present in the aggressive environments of power plants, can be addressed by NiCu-based alloys. Caused by a combination of temperatures around 450–800 °C, a high carbon activity $a_c > 1$, and a low oxygen partial pressure p_{O_2}, coke deposits both at the surface and inside the structure, eventually leading to the destruction of the entire component [13, 14]. Monel alloys can counter this effect as a Cu content of at least 30% catalytically inhibits the sedimentation of C, and thus, no coke layer is formed [13, 15].

Monel alloys have already been manufactured via conventional fabrication processes for more than a century [8]. But besides tool-bound technologies, additive manufacturing paves the way for products that cannot be manufactured in a classical manner and that allow complex undercuts as in extremely fine ribbed heat exchangers for instance. In contrast to conventional manufacturing processes, AM shows good applicability when it comes to low quantity but high complexity issues. Considering the physical state of the input material, AM technologies can generally be split up into the three different categories of powders, liquids, and solids, and against the background of metal materials, powder-based applications are of main interest [16, 17]. According to DIN EN ISO/ASTM 52900, as one of seven process categories for additive manufacturing, powder bed fusion processes locally introduce thermal energy in order to fully melt loose powder particles. Thus, after rapid solidification of the melt, highly dense structures are created. Since a wide range of metal alloys show repeatable good processability, laser powder bed fusion, also known as selective laser melting (SLM), can be considered a promising technology for AM of Alloy 400 [18]. In this iterative process, a layer of powder is applied to a build plate and partly melted by a laser beam, resulting in complex structures with a higher degree of geometrical freedom than in conventional manufacturing.

For LPBF to be a powder bed–based process, suitable material has to be provided. Here, the atomization of bulk Alloy 400 to fine powder plays an essential part in the process route. There are existing several atomization processes within the field of metal additive manufacturing such as water atomization, electrode induction gas atomization (EIGA), the plasma rotating electrode process (PREP), plasma atomization (PA), and vacuum inert gas atomization (VIGA). Among these processes, VIGA leads to a high homogeneity of the melt and the alloying system, respectively. Vacuum and inert gas, such as argon, both prevent the melt from forming oxides with the ambient air, leading to very low oxygen contents of only a few ppm in the alloy. Moreover, an ideal particle size distribution (PSD) for LPBF such as high flowabilities and bulk densities of the powder can be achieved. Also, VIGA is well known for the processing of nonreactive metal alloys which is why, in summary, this atomization process is suited best for the production of Alloy 400 powders [19, 20].

During atomization, when it comes to the exact place of the inert gas introduction, two different set-ups may be applied: free-fall atomization (FFA) or close-coupled atomization (CCA). The former method gives the melt a chance of falling out of the crucible nozzle into the atomization chamber. After a defined distance, the gas stream hits the melt stream, atomizing the alloy to spherical powder that reveals a log-normal PSD [21]. During the latter method, the powder is atomized just as it exits the crucible nozzle. The gas stream rapidly cools down the melt, resulting in a local low-pressure area that further increases the melt volume rate (MVR; MVR = cm^3/10 min). High homogeneities and purities can be reached by application of CCA [21, 22].

When setting up an experiment, there are several methods that can be applied. A classic approach would be the one-factor-at-a-time (OFAT) strategy. This approach, which dates back more than a century, is still used frequently in modern science although not being the most promising one as it is very time-consuming and only varies one parameter at a time. In contrast, a design of experiments approach has the ability to vary several parameters simultaneously, resulting in a more detailed overview of parameter interdependencies in less time. Here, on the basis of multiple input variables, a prediction of the system response can be carried out [23]. In general, DoE requires fewer resources, the prediction for a single parameter is more accurate, interconnections in between parameters cannot be determined with OFAT, and the optimal response of a system is located more precisely [24]. There are many DoE techniques that can be applied to different optimization cases, but they all require a design space as an input, which indicates the spectrum of the variability of one parameter. Conclusions from this input may explain alterations in the output data [25]. The full factorial method is a widely known one with the big advantage

that it can clearly differentiate between single parameters, and therefore, clear conclusions of the respective effect of a parameter on the whole system can be drawn [25–27].

Developing usable material for AM in general and for LPBF in particular comes with some difficulties; the desired state and shape of the feedstock material have to be producible, key properties such as sufficient flowability and bulk density need to be ensured, and the chemical composition must be consistent and free of any impurities [28]. Moreover, defect formation of powders, e.g., in terms of satellite formation or lack of sphericity, has to be avoided as it negatively affects absorptivity and recoatability during printing [29]. Hence, finding a consistent procedure in powder and material development for any alloy to be used for LPBF is essential for the adaptation of the technology. Although numerous processes for gas atomization and laser powder bed fusion of metals are already known, there is no holistic approach for Alloy 400 at this point. The complexity of the atomization of high-melting alloys and the challenges associated with LPBF processing of conductive materials are the main reasons for this. Hence, this study aims to establish such an AM process routine to serve as a standard reference for the present alloy system. This includes material supply via gas atomization, parameter definition according to a design of experiments, and LPBF production of components. Throughout the whole process, powders and parts were analyzed on their microscale, including grain structure and chemical composition. Mechanical properties in terms of indentation hardness and tensile strength were quantified. Not least due to its wide applicability in industrial applications, there is an exigent need to qualify this alloy for the LPBF process. By putting a special focus on reproducibility and unambiguous comparability to hot-extruded reference material (provided by Cunova GmbH), this demand is intended to be satisfied. In order to reach this goal, an emphasis was put on the following novelties:

– Development of a well-adjusted atomization routine, including extensive powder investigations for Alloy 400
– Elaboration of a DoE approach tailored to the Alloy 400 LPBF process, reaching for the highest densities possible
– First-time identification of material characteristics of the additively manufactured Alloy 400 and comparison to conventional fabrication

2 Experimental procedure

2.1 Gas atomization

For the production of metal powder prior to the AM process, an Indutherm Blue Power AU3000 gas atomizer was utilized. Due to its high atomization temperature of ~ 1600 °C

(liquidus temperature: ~ 1350 °C), Alloy 400 can only be atomized using a high-temperature (HT) equipment setup; the bulk material got loaded into a ceramic crucible which itself was applied to a graphite susceptor as displayed in Fig. 1. The heating was done via induction, and a close-coupled atomization setup was used with argon as inert gas. The CCA setup causes the formation of a low-pressure area beneath the nozzle and in combination with the low viscosity of the melt, achieved by considerable overheating, and high gas stream velocity; this leads to the formation of relatively fine particles [30]. During atomization, the Ar pressure was set to ~ 8 bar, and the gas flow was ~ 215 m³/h. In literature, the hereby resulting cooling rates vary from 10^2 to 10^8 K/s [30, 31]. For a powder fraction from 20 to 63 μm, which matches approximately the desired range in this work, more precise cooling rates of 10^3 to 10^4 K/s are stated [32, 33]. In order not to freeze the nozzle with Ar gas and to ensure a sufficient discharge of the liquid, the gas stream was activated with a delay of 1.5 s post to the release of the melt. To further homogenize the material, the liquid Alloy 400 was held at its atomization temperature for 15 min before releasing the melt into the atomization tower. Moreover, low viscosity and, thus, more effective mixing of the melt were ensured by overheating the system by ~ 250 °C above its liquidus temperature. This way, 10 kg of bulk material was atomized to powder during approx. 2 min.

Considering LPBF fabrication capability, the powder being too coarse was sieved out, and particles being too fine were air-separated from the final fraction of 15–63 μm by using an automated sieve (EOS/Russell) and an AC1000 air
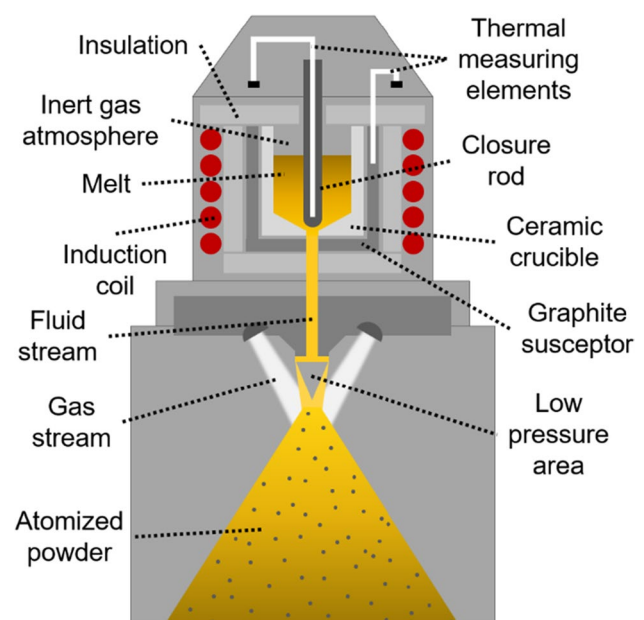
Fig. 1 High-temperature close-coupled atomization setup according to [34]

classifier (Indutherm Blue Power), respectively. The final powder was analyzed by a Zeiss Auriga scanning electron microscope (SEM) in terms of particle size, microstructure, and porosity. By application of a focused ion beam (FIB), cross-sections of particles were analyzed for their grain structure, utilizing Ga^+ as the respective liquid metal ion source. Moreover, the existing elements were classified in greater detail via the application of energy-dispersive X-ray spectroscopy (EDS), using Aztec software (Oxford Instruments) for evaluation. The chemical composition of the powder used for LPBF was double-checked by wet chemical analysis (WCA, Agilent 5800 ICP-OES) and compared to the initial composition of the bulk material. Hall flow testing was performed in order to verify the flowability (DIN EN ISO 4490) and bulk density (DIN EN ISO 3923–1) of the powder. The measurements were extended by powder rheology investigations using a FT4 universal powder rheometer (Freeman Technology) according to ASTM D 7981 at the Research Institutes of Sweden (RISE). These shear cell investigations consisted of flow function, cohesion, Hausner ratio, and surface area. To quantify the particle size distribution with dynamic image analysis (ISO 13322–2), a Camsizer X2 (Retsch) was used.

2.2 Laser powder bed fusion

Throughout the whole laser powder bed fusion fabrication and optimization process, an EOS AMCM M290 customized machine was used. Special features of this machine are a heatable build plate (up to 500 °C), a reduced build space (diameter 100 mm, height 100 mm) for small batch investigations, and a green laser source (wavelength 532 nm). A brush was used as a recoater, and the build chamber was pressured with Ar inert gas. One layer had a thickness of 20 μm, the build plate was pre-heated at 80 °C, and a rotating scanning strategy of 67° was applied. Moreover, the travel of the laser was always directed against the inert gas stream. This way, ejections from the melt pool onto the unmolten powder bed, due to acceleration caused by the gas flow, were prevented. As a test geometry, cubes with an edge length of $8 \times 8 \times 8$ mm^3 (1.5 mm of support beneath) were examined. In total, 24 cubes were fabricated within one build job. Support structures beneath the cubes allowed heat transferability from the part to the build plate and vice versa, as well as easy removal from the build plate by either band sawing or wire electrical discharge machining. The build plate was made of 1.0050 (E295) plain carbon steel and had a round shape with a diameter of 100 mm.

The resulting relative densities were obtained via buoyancy according to Archimedes and optically via light optical microscopy (LOM), respectively, as per VDI 3405–2. As stated in this standard, the first method leads to a quite accurate overview of the overall density of a part, while optical

investigations provide more meaningful insights into the arrangement and form of pores in one specific layer. For this reason, densities measured according to both procedures were considered: buoyancy for a fast, approximate value and optical microscopy evaluations for the more accurate final value. Five areas of a single layer of DoE cubes were considered for the calculation of the average relative density within one specimen. Images of cross-sections parallel and perpendicular to the build plane were taken and compared. They showed no significant difference in terms of density in between each other, and thus, parallel preparation was chosen for the evaluation of optical density due to faster preparation. LOM images were taken by a digital microscope (Keyence), and the ImageJ software was used for the determination of density. Also, specimens were etched with ferric chloride in order to make visible the melt pool propagation in the build direction under the LOM.

For examinations via SEM, cubes were cut in half perpendicular to the build plane by a linear precision saw IsoMet 4000 (Buehler) and fixed in a conductive-filled phenolic mounting compound, using a warm embedding device SimpliMet 1000 (Buehler). Afterwards, parts were ground (down to 2500 grit SiC paper) and polished (down to 0.02 μm colloidal silica suspension) by an EcoMet 300 (Buehler). Chemical analysis was carried out by wet chemical analysis and double-checked by application of EDS. The grain structure was investigated by electron backscattered diffraction (EBSD). For more in-depth characterization of the nanoscale, a transmission electron microscope (TEM) JEOL JEM-2100F working at 200 kV was used. It was operated at the Institute of Physics of Materials, Brno, and it is equipped with a bright-field detector allowing observation in scanning mode (STEM) as well as an Oxford XMAX80 EDS detector for analysis of the local chemical composition.

2.3 Material properties

In order to obtain the mechanical properties of the LPBF-fabricated alloy, tensile tests according to VDI 3405–2 were performed. A universal electromechanical Zwick Z050 tensile testing machine was used with a strain rate of 8.0×10^{-3}/s. The elongation was detected via sensor arm extensometers. Cylinders for tensile testing had a diameter of 10 mm and were reworked by machining, resulting in type B specimens as per DIN 50125 (diameter 6 mm, gauge length 30 mm). As recommended in the standard, blanks were built in three different orientations:

– In a polar angle Θ of 90° to the build direction (horizontal orientation in build space)
– In a polar angle Θ of 45° to the build direction (diagonal orientation in build space)

– In a polar angle Θ of 0° to the build direction (vertical orientation in build space)

All blanks revealed an azimuth angle φ of 45° to the coater brush. This angle was chosen in order to ensure proper coverage of the melt pool with every new layer of powder. For hardness measurements, $8 \times 8 \times 8$ mm^3 cubes were manufactured and ground on the test surfaces (parallel as well as perpendicular to the building plane). Hardness was then obtained according to Vickers as per DIN EN ISO 6507–1.

Tensile tests were also carried out at elevated temperatures at the Institute of Physics of Materials, Brno, in order to further investigate the behavior of the alloy in possible high-temperature fields of application. For this purpose, small cylindrical specimens (3 mm in diameter, 9 mm in gauge length) were used. The specimens were fabricated from a material block prepared by additive manufacturing; the specimen axis was perpendicular to the building direction ($\Theta = 90°$). A universal electromechanical Zwick Z050 system was used in the regime of constant traverse speed (1 mm/min, which corresponds to a strain rate of 1.6×10^{-3}/s). The ductility was measured by a clip-on extensometer with ceramic rods (MayTec), touching the specimen. The furnace was equipped with 3 thermocouples for controlling the temperature stability and keeping a low thermal gradient. Tests were performed in laboratory air.

2.4 Design of experiments

To be able to find a LPBF parameter set that exceeds high densities of 99.5%, a DoE approach using Minitab software was carried out and applied to the optical density data taken from cross-sections of specimens. As parameters, laser power p_L in (W), scanning speed s_S in (mm/s), and hatch distance d_H in (μm) were investigated. They all affect the final density of the part in a significant way, and their interdependency can be described by a cube, consisting of a dark blue center point, orange corner points, and light blue star points (Fig. 2). The center point describes the input data, taken from previous studies and/or iterations. With the help of corner points, a space is built up around the center point which is likely to contain a better response in terms of density. Several combinations of input variables fluctuate in a positive and negative manner around the starting values of the center point. Ultimately, star points are reaching out of the cube, representing extreme values of one parameter only, while the other two stay at their center point levels. Single-parameter influences can be derived from this.

Three DoE iterations were carried out to narrow down further the parameter ranges needed to reach the goal of high density. However, before processing the first DoE iteration, the program needed initial information about the
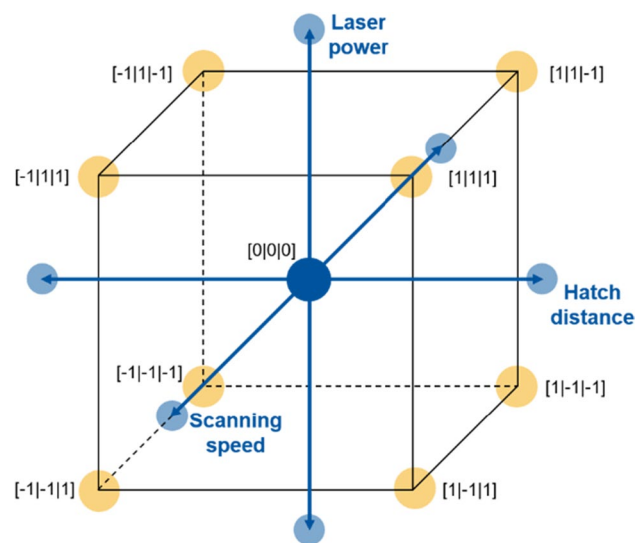
Fig. 2 Laser power, scanning speed, and hatch distance within the design space

input–output interdependence. Therefore, the very first print job was carried out without the use of software but based on parameter sets that showed good processability for different yet comparable alloys, such as Alloy K500. By finding the correlations between parameter combinations and resulting densities, the computational simulation was filled with data. As a result, new parameter settings were calculated and interpreted, leading to higher densities throughout the first DoE iteration. The maximum attainable density rose from one iteration to another, but ultimately, the optimization would stagnate, revealing no significant improvement of a new parameter set when compared to the previous one. This indicated the end of the procedure.

3 Results

3.1 Powder production and characterization

The chemical composition was determined for gas-atomized powders, LPBF-fabricated parts, and hot-extruded reference samples by wet chemical analysis and EDS, respectively. Results and face values according to DIN 17743 (material no. 2.4360, NiCu30Fe) are given in Table 1. For carbon being a light element with a very low proportion in the present alloy, measurements were excluded due to unreliable detectability.

With respect to the chemical requirements of Alloy 400, no significant deviations were detected for LPBF-fabricated parts throughout the whole process. Moreover, when comparing powders and LPBF specimens, only small variations were measured. Due to this analytical evidence, the

Table 1 Intervention limits of Alloy 400 and measured compositions according to application of wet chemical analysis and energy-dispersive X-ray spectroscopy in different states (in wt. %)

Chem. element	Ni	Cu	Fe	Si	Mn	Al
Nominal composition	≥ 63.0	28.0–34.0	1.0–2.5	≤ 0.5	≤ 2.0	≤ 0.5
Reference (WCA)	62.5	31.4	2.2	0.2	1.3	0.1
Reference (EDS)	62.3	29.7	2.0	0.3	1.1	0.2
Powder (WCA)	63.2	31.6	1.9	0.2	1.0	0.2
Powder (EDS)	63.2	28.6	2.1	0.3	1.1	0.3
LPBF (WCA)	64.1	31.0	2.4	0.2	1.3	0.2
LPBF (EDS)	63.4	30.1	2.1	0.4	1.1	0.3

processing of gas-atomized powder was considered to fulfill the specification. Analyses on reference samples were to a great extent in line with the standard as well.

Further SEM investigations of the powder were carried out with a secondary electrons secondary ions (SESI) detector, and results are displayed in Fig. 3a. Gas-atomized Alloy 400 reveals mostly spherical particles with only sporadic occurrence of satellites or coarse agglomerates, which would negatively influence powder processing properties, in particular its flowability [35, 36]. The images clearly indicate the rapid cooling of the particles during atomization, resulting in very fine, dendritic grain growth and grain sizes of approx. 1 to 9 μm (mean 5.2 ± 3.2 μm). Small powder particles tend to evolve small grains of a few micrometers only, and larger particles show coarser grains of up to 15 μm. Figure 3b shows a single powder particle that was cut with a focused Gallium ion beam. Having a more detailed look at single grains and grain boundaries with the in-lens detector, no precipitates of the associated elements were detected, being in line with the assumption of this alloy being a solid solution [1]. Nevertheless, having a closer look at EDS data,

a special property of Alloy 400 was detected; the concentration of copper is higher at the grain boundaries than within the grains and vice versa, and the concentration of nickel is lower at the grain boundaries than within the grains. These local differences in concentration were classified as segregations, which are typical for NiCu-based alloys [37–39]. Segregations concerning the remaining five elements were not detected. Furthermore, no gas porosity or impurity was detected within the particles. Such defect-free particles with fine grains are considered favorable for production as stated in [31, 40]. In general, the chemical distribution of elements can be described as homogeneous, both on the surface of and inside the particles, respectively.

On average, the volumetric sphericity measured by dynamic image analysis reached a normalized value of $spht_3 = 0.766$ (1.000 being perfectly spherical). Even though most particles appear spherical in SEM, a lower $spht_3$ was attributed to the few attached satellites, as documented in [41]. Volumetric symmetry ($symm_3 = 0.916$) and volumetric aspect ratio of width to length ($w/l_3 = 0.821$) correspond to this observation. This indicates that the powder is probably
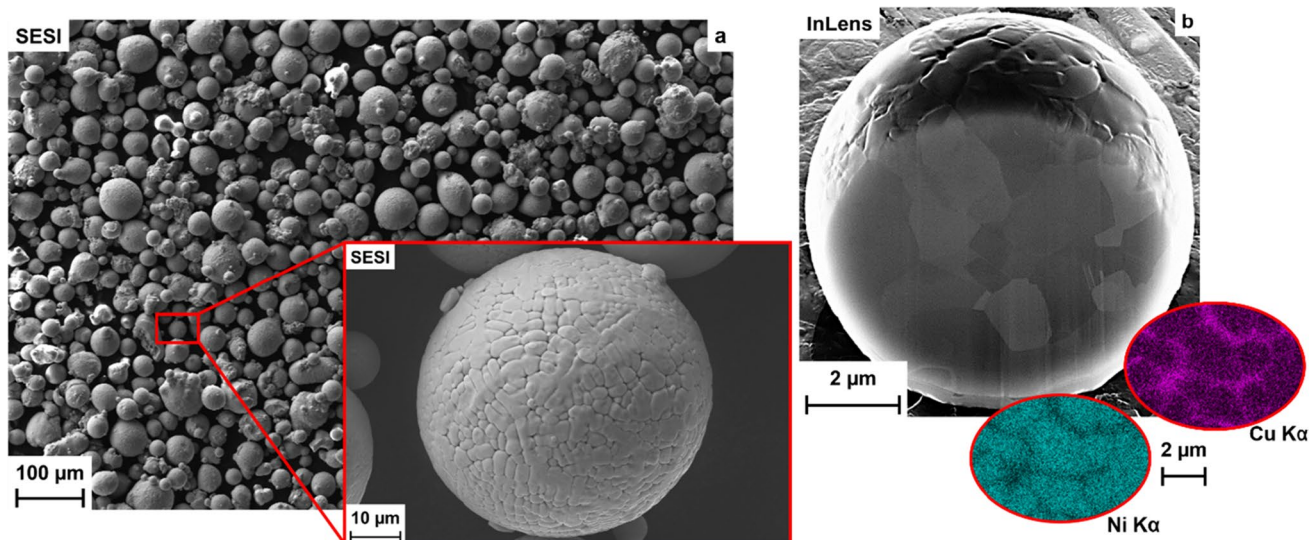
Fig. 3 **a** SEM micrograph of gas-atomized powder (overview and detail); **b** a FIB cross-section of a single particle, illustrating grain growth and, via application of EDS, Cu segregations at grain boundaries
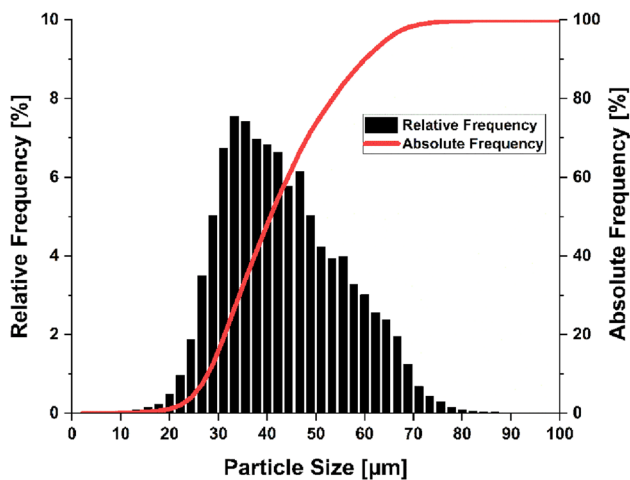
Fig. 4 Particle size distribution of the final powder fraction used for LPBF printing

processable as key values close to 1.000 are linked to a high flowability of the powder and great energy absorption of the laser into the particles [42, 43]. Powder being too coarse was sieved out by a sieve with a mesh size of 63 μm. The remaining fraction was then air-separated in order to remove particles being finer than 15 μm. This way and as displayed in Fig. 4, the particle size distribution could be narrowed down to a Q_3 (10%) of 28.9 μm and a Q_3 (90%) of 61.5 μm; the Q_3 (50%) was 42.3 μm and in line with the qualitative findings via SEM. The bulk density of the final powder fraction was $\rho_b = 4.38$ g/cm^3, indicating a relative density of $\rho_{rel} = {\sim}50\%$ when compared to the nominal density of Alloy 400 ($\rho_n = 8.80$ g/cm^3) [7]. With a Hall flowability of 15.22 s per 50 g powder, the particles showed a good mass flow; ratholing phenomena were not observed, and the standard funnel did not have to be knocked at in order to initiate the flow. A good flowability was attributed to the high sphericity of the particles [44]. Shear cell investigations were performed after conditioning the powder with a pressure of 9 kPa. By twisting one layer of powder relative to another one, a flow function $FF = \sigma_M/\sigma_C$ was calculated with σ_M being the major principal stress and σ_C the unconfined yield strength. A normalized flow function value of approx. 15 was detected, with values above 10 being considered as flowing well according to the specifications of the device manufacturer (Freeman Technology, 2023). This is underlined by the low degree of cohesion of ${\sim}0.25$ kPa of the powder when being sheared. Moreover, the Hausner ratio as an indicator for the attrition in between particles was 1.09 for the present Alloy 400, which is desired in terms of processability [45–47]. On average, the surface area of the coarse powder measured 0.034 m^2/g.

The above results led to the conclusion that the powder should behave as expected during LPBF, which meant that it could be applied properly to the powder bed and that processability was generally ensured.

3.2 Laser powder bed fusion and design of experiments

3.2.1 Parameter optimization

Throughout the LPBF process parameter optimization, the parameters were varied as follows:

– Laser power p_L: 60–120 W.
– Scanning speed s_S: 250–1350 mm/s.
– Hatch distance d_H: 30–120 μm.

Considering a single DoE iteration, the simulation needed to be interpreted against the background of input–output correlations, exemplary as displayed in Fig. 5. This figure can be considered as a two-dimensional cut through the cube presented in Fig. 2. The parameter setting revealed a constant value for the hatching distance (80 μm) and variations in the other two: scanning speed (600–1300 mm/s) and laser power (60–110 W), respectively. On the basis of density measurements and allocation to the set parameters (black dots), calculations were performed that predicted the occurrence of different, pre-defined density ranges (shades of green). In this particular case, no densities above 99.5% were predicted for a constant hatch distance of 80 μm, regardless of how much the other two parameters were adjusted. A hatching of 80 μm is therefore generally considered unsuitable in order to reach high densities. Hence, the investigated process window did not show sufficient measuring points at this stage and needed to be investigated for other hatch distances.
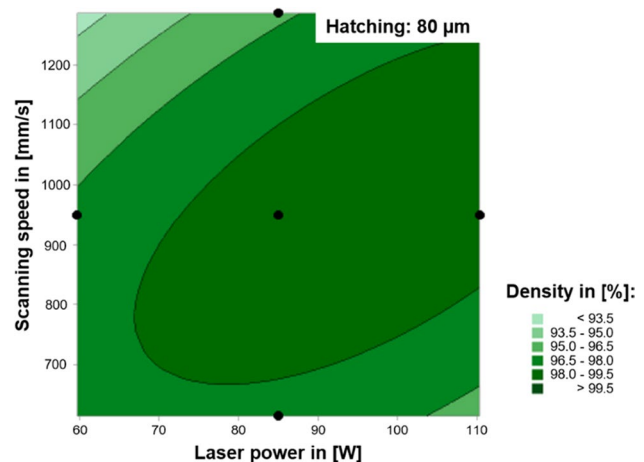
Fig. 5 DoE contour diagram for varying laser powers and scanning speeds at a constant hatching distance of 80 μm, expected density ranges in shades of green
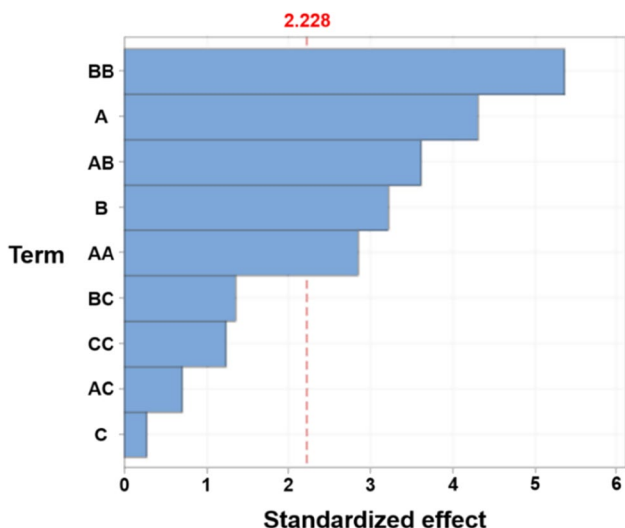
Fig. 6 Pareto diagram of standardized effects revealing the statistical significance of the parameters laser power (A), scanning speed (B), hatch distance (C), and their combinations

With density being the output variable of the regression equation, a Pareto diagram of standardized effects as in Fig. 6 was drawn from the parameters. For A being the laser power, B being the scanning speed, and C being the hatch distance, the diagram clearly indicates statistical significance for A and B as they cross the reference line of 2.228 in whatever combination (A, B, AA, AB, BB). The reference value varies from one iteration to another as it results from the respective regression equation of one iteration. The value is affected by the linear term, the quadratic term, the two-factor interaction, and the error term. The linear term illustrates the effect of a single parameter only, while the quadratic term acts as a balancing calculation (a more accurate replica of the answer term). For variable C, hatching, no statistically significant term was found with respect to the parameter combinations displayed in Fig. 5. This underlines the need for further testing and evaluation of the influence of the hatch distance. The factors are statistically significant at the $\alpha = 0.05$ level, which meant that the probability of the displayed results being not due to the investigated relationships is below 5%.

According to [48, 49], the nominal energy introduced into the part (neglecting reflection) can be described by

$$e_V = p_L / (s_S * d_H * t_L)$$

with e_V being the volume energy density in (J/mm^3) and t_L the thickness of a layer in (µm) with a constant value of 20 µm. In total, 72 parameter combinations were examined during three DoE iterations. Figure 7 gives an overview of the absolute positioning in the design space consisting of laser power, scanning speed, and hatch distance as well
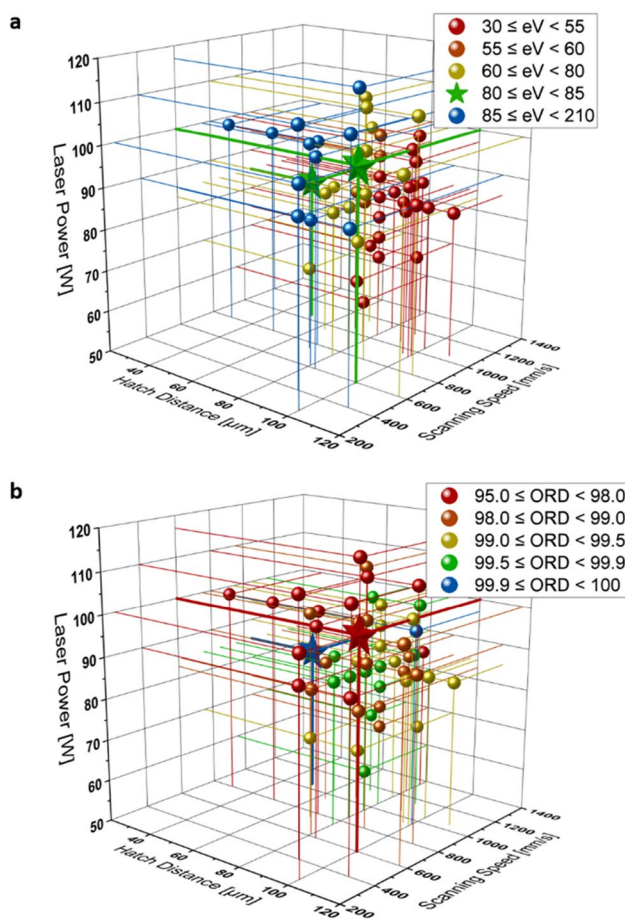

Fig. 7 a Parameter combinations within the design space, color-coded according to their resulting volume energy density in (J/mm^3); **b** same parameter combinations but in turn, color-coded according to their resulting optical relative density in (%)

as relative positioning in between various parameter sets. While Fig 7a indicates the resulting volume energy density, Fig 7b shows the resulting optical relative density (ORD). Parameters leading to similar volume energy densities are colored equally with an e_V of 210 J/mm^3 being the maximum tested one. It can clearly be observed that border areas like 0 to 55 J/mm^3 and 85 to 210 J/mm^3 are distributed widely throughout the design space, while an energy density of 60 to 80 J/mm^3 leads to a rather marginal distribution around the common core of the examined parameter sets. There are only two parameter combinations belonging to the category of 80 to 85 J/mm^3, indicated by two green stars. The lower left star represents an e_V of 80.95 J/mm^3, originating from $p_L = 85$ W, $s_S = 1050$ mm/s, and $d_H = 50$ µm. For the upper right star, $p_L = 100$ W, $s_S = 600$ mm/s, and $d_H = 100$ µm were the parameters, resulting in an e_V of 83.33 J/mm^3. Both stars are highlighted concerning their ORD as well, once as a blue star with an ORD of 99.94% and once as a red star with an ORD of 97.26%.
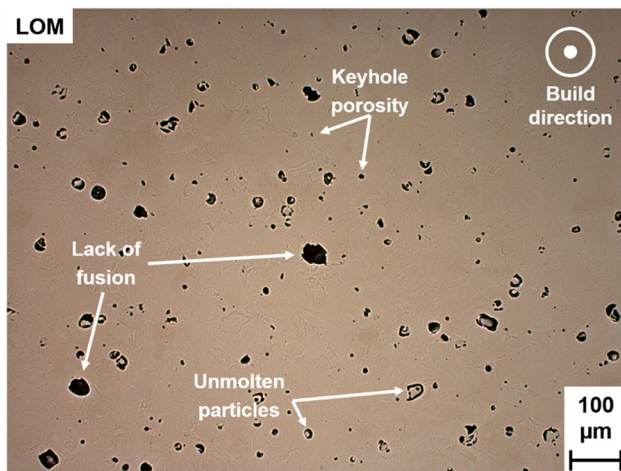
Fig. 8 Non-adjusted parameter set "red star," leading to pronounced pore formation
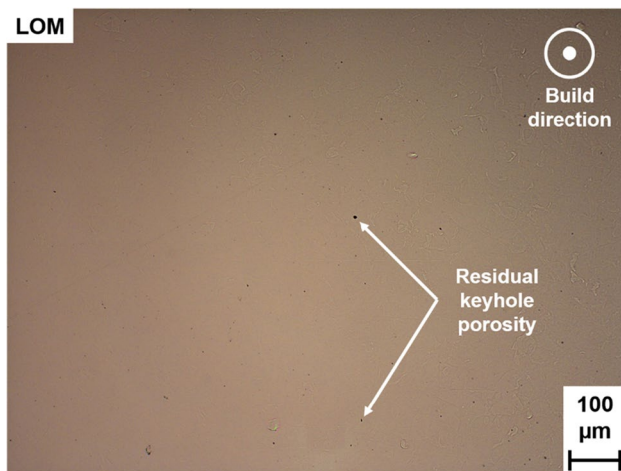
Fig. 9 DoE-adjusted parameter set "blue star," revealing a significant increase in part density

3.2.2 Optical density

Representing the above-mentioned "red star," Fig. 8 shows a cross-section perpendicular to the build direction. Since the parameters were not coordinated with each other, high porosity occurred, leading to multiple defect formation. According to [50, 51], present defects were described as a profound lack of fusion and unmolten powder particles, both originating from low energy density, and fine keyhole formation, originating from high energy density.

For Fig. 9 instead, representing the "blue star," very little pore formation occurred during LPBF. The existing pores were considered keyholes, resulting from fine shielding gas inclusions during re-solidification of the material and vaporization of the melt [50–52]. Comparing both the "red star" and the "blue star," it was observed that highly similar volume energy densities led to highly different optical relative densities.

3.3 Part characterization

3.3.1 Microstructural analysis

Following the parameter optimization process, samples with the highest achievable densities were selected to be investigated for their microstructure, and comparisons to conventional materials were drawn. Having a look at the polished *xy*-plane of the LPBF specimen (view from the top, perpendicularly to the build direction) by operation of a back-scattered electron detector (BSD), as displayed in Fig 10a, small cellular grains with a maximum length of 50 μm were detected, while most of the grains were even finer (~16.5 μm on average). This particular layer revealed an orientation of the laser travel paths (yellow lines) of ~35° tilted against the nominal of the plane. Nevertheless, as a rotating scanning strategy was applied to other layers, different rotation angles have been found. The orientation within one single *xy*-layer varies along the *z*-axis throughout the whole part. When investigating the parts in parallel to the build direction (Fig 10b), fan-shell-shaped melt pools directed along the *z*-axis became observable, resulting from the iterative (re-) melting and solidification during LPBF in between layers, as described in [53]. An orientation along the build direction is a common phenomenon of LPBF-built parts that can be explained by the extreme temperature gradients occurring during fabrication and the resulting directed solidification [54, 55]. Moreover, the width of the laser beam focus of approx. 50 μm was detected (yellow lines). The shell shape of single melt pools and the solidification orientated in the build direction were confirmed by an EBSD mapping (Fig 10c). It also revealed a slight crystallographic <101>texture of the fcc unit cell parallel to the build direction. The corresponding inverse pole figure for the build direction (IPF Z) underlines this finding as the [101]-orientation is highlighted in red with a standardized maximum of 1.77. IPF Z was retrieved in the associated <100>pole figure (PF), highlighting the respective [101] texture uniformly around the [100] center at approximately 45°. In contrast to this, the texture of grains perpendicular to the build direction is randomly and evenly distributed; a clearly preferred orientation for IPF Z was not observed in the IPF X (Fig 10d) and IPF Y (Fig 10e) mappings.

In comparison, the grain structure of the hot-extruded, recrystallized material was substantially coarser and reached grain sizes of up to 200 μm (Fig. 11). No directed solidification could be observed, and grains appeared in an equiaxed state. Hence, by a factor of approximately 10, LPBF-fabricated parts revealed a much finer grain structure.
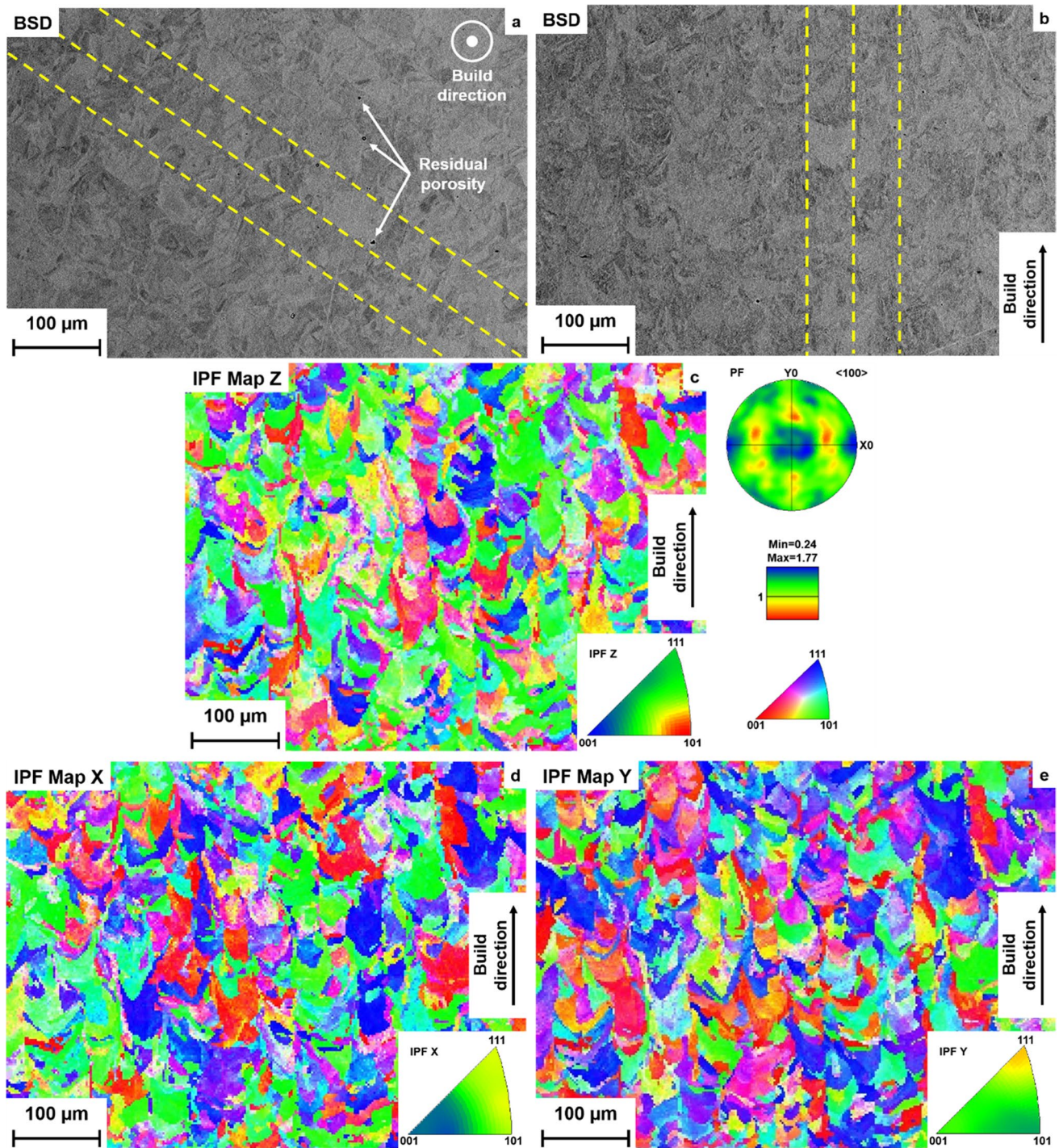
Fig. 10 **a** BSD of LPBF-printed specimen perpendicular to the build direction; **b** BSD parallel to the build direction; **c** Z EBSD mapping, IPF Z, PF for the build direction, color intensity bar and color code triangle; **d** X EBSD mapping and IPF X; **e** Y EBSD mapping and IPF Y

Micro-dendritic structures as well as high dislocation densities are a common, well-studied phenomenon of LPBF-produced parts in as-built conditions, resulting from the high cooling-melting ratio [56–62]. Accordingly, these internal structures were also detected in this work as shown in Fig. 12. Micro-dendritic cell structures, revealing a cell size of approx. 250–500 nm, accumulate in between grain and sub-grain boundaries and are intersected by a wide variety of dislocations. The dislocations, which to some extent compensate for the immense internal stresses due to rapid temperature changes during production, are
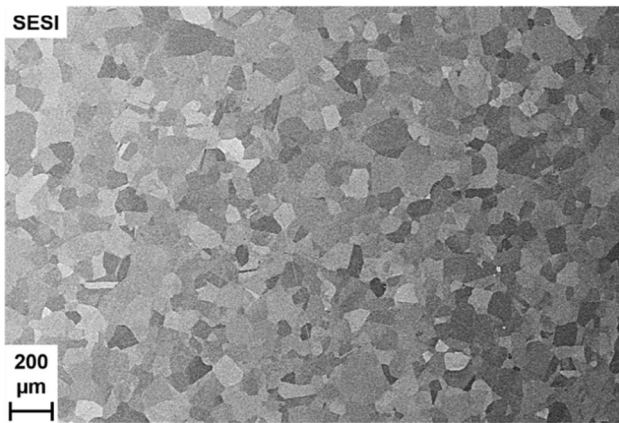
Fig. 11 Recrystallized reference material revealing a coarse, equiaxed grain structure, detected by SESI

mainly focused on the cell walls and to a lesser extent are also present inside these cells.

3.3.2 Mechanical properties

In order to quantify the mechanical properties of additively manufactured Alloy 400, tensile tests at room temperature were carried out on specimens that had been printed in different polar angles according to the DoE-optimized parameter set: perpendicular (90°), diagonal (45°), and parallel (0°) to the build direction. Tensile test specimens revealed an ORD of 99.56% on average. As displayed in Fig 13a, for parts that were printed in horizontal orientation, ultimate tensile strength R_m and yield strength $R_{p\,0.2}$ showed maximum values of 615 MPa and 556 MPa, respectively. Tensile specimens with a polar angle of 0° showed minimum values instead ($R_m = 592$ MPa and $R_{p\,0.2} = 519$ MPa, respectively). Therefore, tensile strength and yield strength decreased when the specimen axis approached the build direction (upright specimens). Young's modulus E revealed a clear maximum of 159 GPa for 45° built geometries and lower values for the other two orientations (90°, 133 GPa; 0°, 135 GPa). In Fig 13b, elongation at break A_5, uniform elongation A_g, and fracture necking Z are displayed. A_g showed a certain tendency, the smaller the polar angle, the stronger the elongation (90°, 3.0%; 45°, 3.6%; 0°, 3.7%). Also, $A_5 = 11.7\%$ and $Z = 28.9\%$ had their minima at 90°, respectively, leading to the observation that the ductility of the alloy increased with parts being printed more upright/vertically in the build space. These findings are in line with the above-described decline of R_m and $R_{p\,0.2}$ from 90 to 0° oriented parts; the smaller the polar angle (speaking the more upright the part is orientated in the build space), the lower the strength and the higher the ductility within the part.

Further tensile testing on specimens fabricated perpendicularly to the build direction was carried out at elevated temperatures, and a comparison to conventionally fabricated
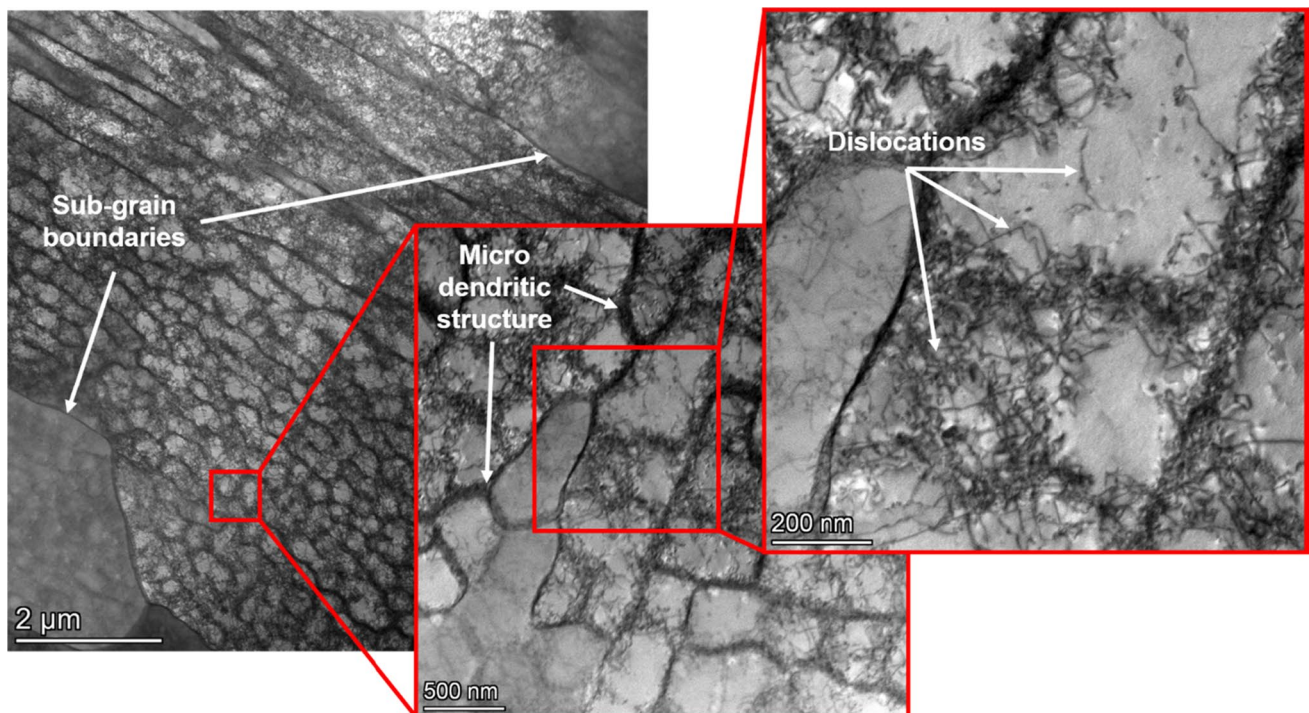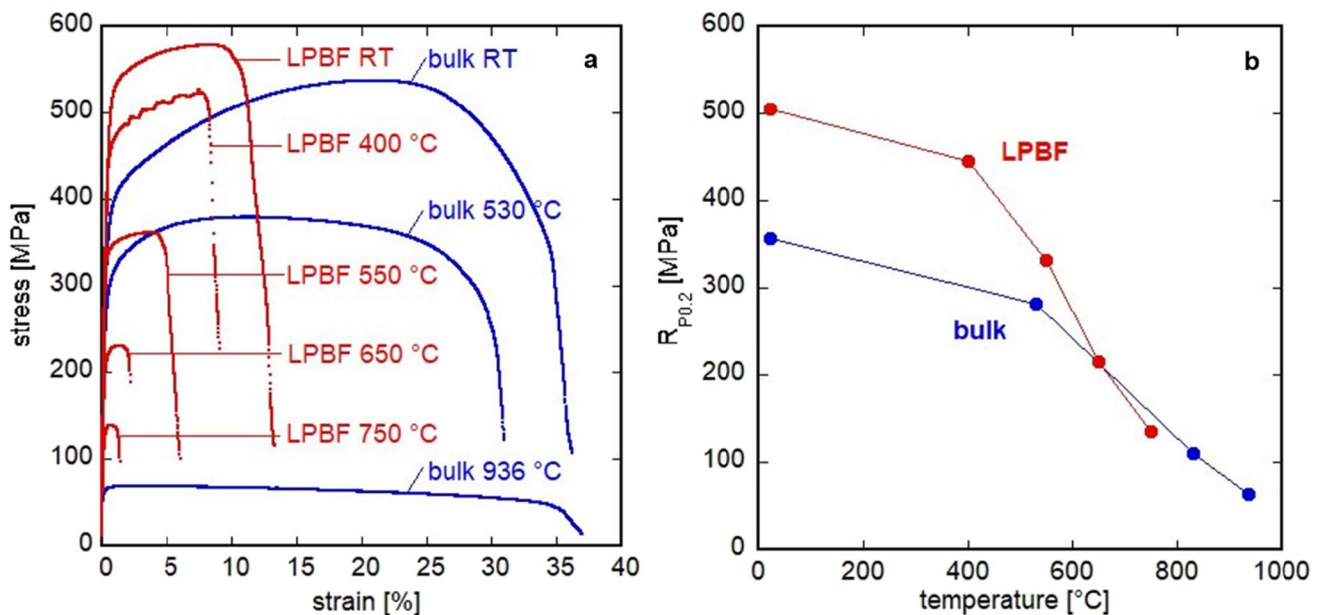

Fig. 12 Bright-field STEM micrographs revealing grain and sub-grain boundaries and internal micro-dendritic structures with high dislocation density in wall segments and dislocation-free center
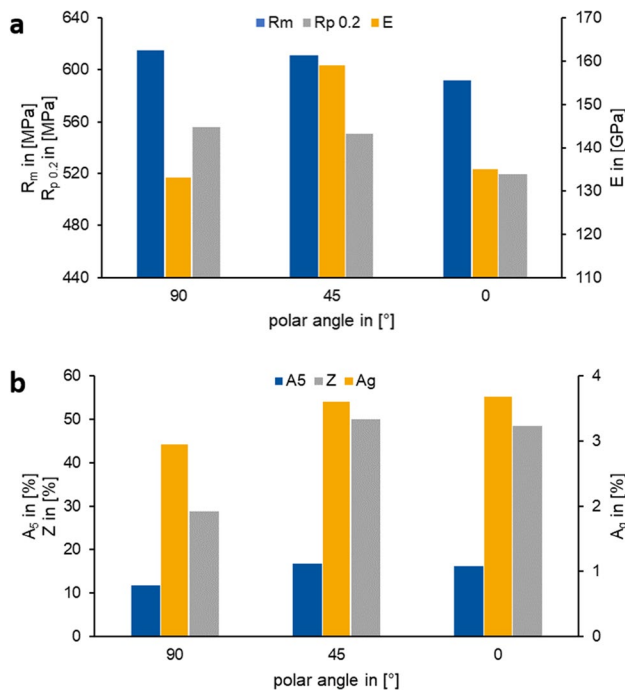
Fig. 13 **a** Stress and Young's modulus for LPBF Alloy 400, printed in different orientations; **b** strain and necking

the yield strength on the testing temperature. The tensile strength and yield strength of the LPBF part were similar or higher in comparison to the bulk variant. However, the elongation at fracture of the LPBF variant was substantially lower with a tendency to decrease with rising temperature.

Concerning hardness, cubes were evaluated in parallel and perpendicular to the build direction; no difference was observed here. Moreover, results for micro- and macro-hardness were identical. On average, the samples showed a hardness according to Vickers of 194 HV1 and HV10, respectively. For conventionally fabricated material (annealed condition), a hardness of ~107–147 HV1 was stated, while hot-rolled and hot-finished parts may reach similar hardness values as the LPBF variant [1, 7]. Hot-extruded material, as used throughout this study, shows an HBW 2.5/62.5 of 115–121. Higher hardness in the LPBF variant was traced back to the finer grain structure, as discussed in [2].

4 Discussion

4.1 Powder suitability for LPBF

The atomization process window was considered suitable in terms of an effective operation of the low-pressure area, leading to the desired rapid undercooling of the melt. Fine powders resulted, porosities and impurities were not detected which would be detrimental for the LPBF process [63, 64]. It was possible to create spherical particles showing only a small number of satellites, resulting in high flowabilities

Alloy 400 was drawn. The resulting tensile curves are shown in Fig 14a. LPBF parts were tested at room temperature, 400 °C, 550 °C, 650 °C, and 750 °C (red lines). For the hot-extruded, bulk parts, room temperature, 530 °C, and 936 °C were applied (blue lines). Fig 14b shows the dependence of

Fig. 14 **a** Stress–strain-diagram for bulk (blue curves) and LPBF (red curves) Alloy 400 at various temperatures; **b** yield strength as a function of applied temperature

and bulk densities needed for successful AM [64, 65]. As a consequence, this eventually leads to higher build quality during LPBF [63–65]. The resulting fractal nature of the powder bed in the LPBF process was introduced by Estrada-Díaz et al., i.e., as per the fractal dimensions and lacunarity, accurately correlating both homogeneity and morphology with a sustainable, low-defect LPBF process [66, 67]. No precipitates were found within the particles, which is in line with the assumption of this alloy being a one-phase solid solution [1–3]. Besides, Cu segregations were expected and also detected on grain boundaries [37–39]. A consistent chemical composition was found in both, powders and parts, and thus, the generated powder was generally considered appropriate for LPBF.

4.2 Melt pool geometry and resulting microstructure

NiCu-based Alloy 400 is a fcc alloy, and thus, it is expected that the preferred dendrite growth direction is along the [001] crystal direction [68–71]. In the case of LPBF, the thermal gradients are pointed normally to the melt pool boundary, and thus, grains with [001] directions parallel to the thermal gradients will preferentially grow from the melt pool boundary. Attributed to the Gaussian profile of the laser source, the core of the melt pool eventually exhibits higher temperatures than the border areas [68, 71–73]. As frequently observed in other works like [55, 71, 74, 75], due to the geometry of the melt pool, boundary-near grains grow transversely to the direction of the introduced laser power and build direction, respectively. In turn, nucleation near the melt pool core experiences undirected undercooling, leading to the formation of more equiaxed grains. Figure 15 shows the ideal melt pool that would result under these circumstances, consisting of dendrites near the melt pool boundary and of cross-sections of elongated grains resulting from the laser beam travel (here, out of the figure plane). The resulting growth mechanism gives reason for the [101] orientation with respect to the build direction that has been found for the present alloy and manufacturing routine, respectively; dendrites do not only grow along the build direction but deviate into the build plane as well. This type of process-induced deflection of grain growth toward < 011 > orientations was also found for a Ni-based IN718 by Pant et al. and for a NiTi-based alloy by Safaei et al. [71, 76].

Nevertheless, the texture was described as marginal only (Fig 10). This was found to be due to a wide variety of geometries, sizes, and growth directions of the grains, resulting in a very heterogeneous microstructure. In other words, the above-described ideal melt pool was hardly detected within the present LPBF manufactured parts as illustrated in Fig. 16. Melt pool boundaries could be tracked down partially only, and equiaxed and columnar grains appeared
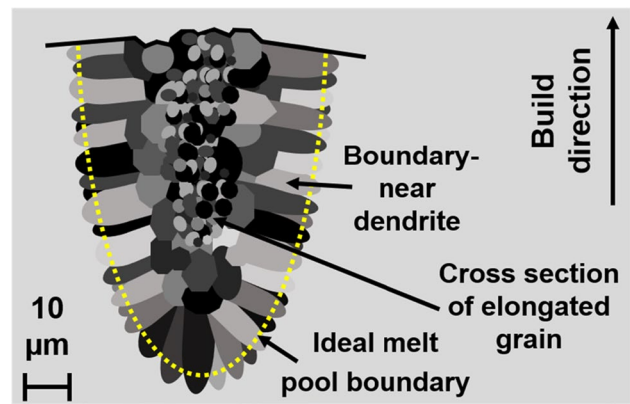

Fig. 15 Schematic of an ideal melt pool, denoting different types of directed grain nucleation
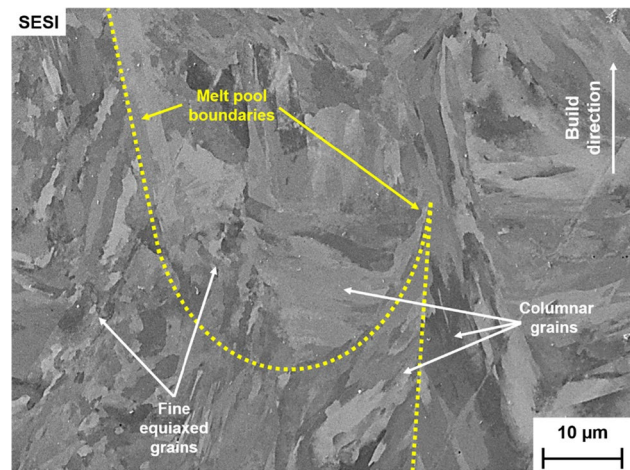

Fig. 16 SEM closeup of the melt pool intersections in between several layers

randomly distributed over the cross-section. This can be related to the rotating scanning strategy; as stated by Serrano-Munoz et al., a rotation of 67° in between layers allows for the formation of both elongated grains along build direction and epitaxial growth [77]. According to Qin et al., this type of rotation lowers the overall texture [55].

Etched with ferric chloride, the melt pool propagation in the build direction (z-axis) was revealed in greater detail (Fig. 17). The pre-described fan-shell shape became even more observable, resulting from an overlapping of melt pools from one layer to another. The ratio of melt pool depth and layer height shows an effect here; with a width of 50 µm, approximately 80 µm was found to be the maximum melt pool depth, while the applied layer height measured 20 µm only. Hence, a melt pool of a considered level reached four layers deep into the part, meaning that the original melt pool geometry of one respective layer was dissolved by the

Fig. 17 Light optical image of an etched slice parallel to the build direction, illustrating overlapping melt pools
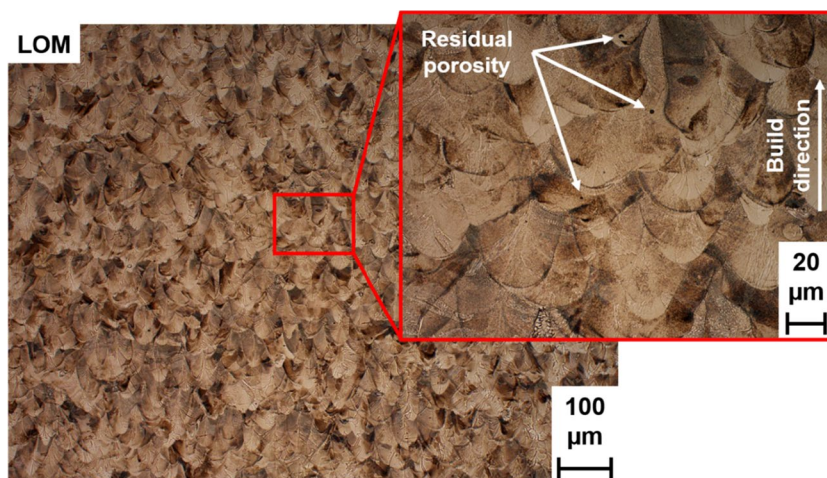

impacts of further melt pools from overlying layers. This, in turn, results in a quadruple (re-)melting and solidification of the material with the heat-affected zone (HAZ) reaching even deeper. The HAZ may further significantly alter the microstructure [78, 79]. These findings serve as another explanation for the above-found very different grain structures and nucleation mechanisms. Apart from that, a few remaining pores were observed on the etched samples, being classified as keyholes.

Copper segregations on grain boundaries were clearly visible for the as-atomized powders (Fig 3). In contrast, using TEM for as-built LPBF parts, chemical micro-Cu-segregations became visible on the nanoscale, revealing a very low intensity at cell walls (Fig. 18). According to Bertsch et al., the occurrence of these micro-segregations can, in some cases, be correlated with the previously mentioned dislocations as these can act as traps for some elements [80]. Sabzi et al. showed that high cell-wall-near dislocation densities significantly enhance the strength performance of the respective alloy, while Kong et al. stated that

high dislocation densities go along with nanosized cellular structures which, in turn, enable superior performance in comparison to conventional manufacturing [59, 60]. These nanocell structures, revealing high dislocation occurrence, have been found for the present LPBF Alloy 400 as well as previously displayed in Fig. 12.

Compared to the one-time rapid undercooling of the melt during powder atomization, the thermal impact on LPBF parts is more complex and caused by an entire sequence of iterative laser melting and subsequent very high cooling rates [68, 81]. As illustrated above (Fig. 18), the respective part layers experience several iterations of melting and solidifying before being additionally exposed to the HAZ during the fabrication of further layers. Also, non-molten powders aside may keep the heat locally concentrated near the melt pool [82]. Hence, an in situ, process-related heat treatment during manufacturing caused by the succession of several layers can be noted, inevitably benefitting diffusion processes based on a temperature gradient. From one layer to another, this eventually results in a decrease of locally
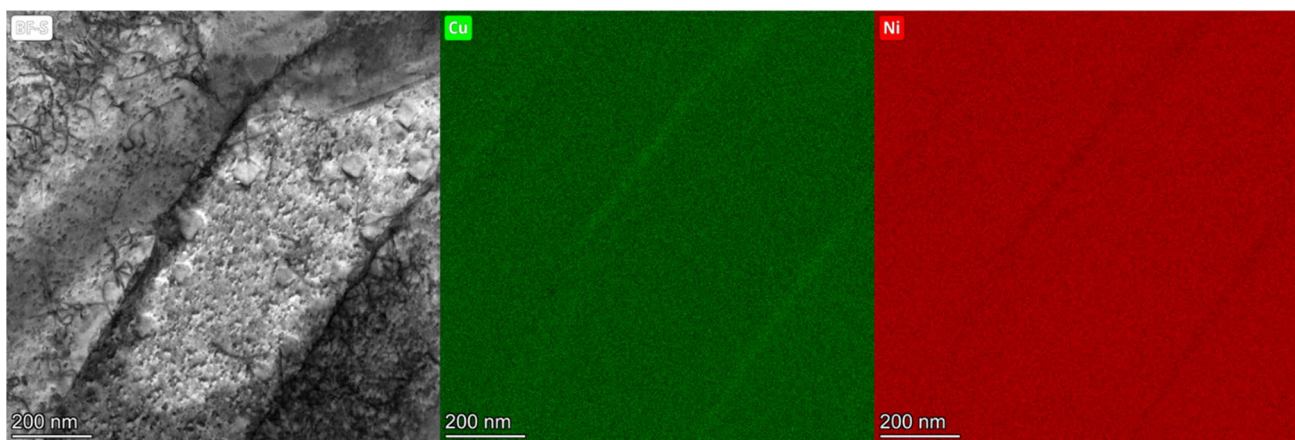
Fig. 18 Bright-field STEM micrograph and micro-segregation of Cu and Ni on the nanoscale as detected by EDS analysis in STEM

different chemical concentrations, and ultimately, inhomogeneities almost dissolve completely into the preferred homogeneous solid solution. This serves as a further explanation for the copper segregations being only detectable on the nanoscale via TEM within LPBF parts compared to the strongly pronounced segregations in powders.

4.3 Building strategy and consequential material properties

Even though chemical imbalances are eliminated within the parts, structural irregularities do remain. Not only that no significant texture was found for the *xy*-plane but solely along the build direction, but there are also differences in mechanical properties concerning the orientations of fabricated specimens. As observed, the ultimate tensile strength and yield strength of tensile test specimens decrease with a falling polar angle from 90 to 0° to the build direction (Fig 13a). In other words, the more upright the cylinders were manufactured during LPBF, the less strength they showed. Keeping in mind the directed grain growth along the build direction, this leads to the assumption that the lateral overlap of melt pools (horizontally in the build space, primarily present in 90° oriented samples) results in a higher strength performance than the overlap of melt pools on top of each other (vertically in the build space, primarily present in 0° oriented samples). Here, the 45° oriented samples are equivalent to a combination of both, vertical and horizontal overlap, resulting in mechanical properties between them. The samples that were tested perpendicular to the build direction showed the lowest levels of elongation (Fig 13b). Accordingly, higher ductility in the build direction was found by Wilson-Heid et al. for a Ti-6Al-4 V alloy, being correlated to the columnar grain growth along the *z*-axis and a consequent damage accumulation in the horizontal direction [83]. Also, Yu et al. found a higher ductility for upright-oriented Hastelloy X samples, mainly attributed to a considerable extent of texture and grain rotation in this direction [84]. These results are consistent with those shown here that the strength is inversely correlated with ductility. This is further underlined by the low fracture necking for 90° oriented samples. Thus, strength and ductility are evolving contrarily with the Young's modulus being the highest for the diagonally oriented specimens. This anisotropic behavior of Young's modulus in LPBF with accompanying varying stiffness values depending on the orientation of the specimen has been frequently discussed in literature like [84–86]. Ultimately, anisotropy along the *z*-axis was found, while for single *xy*-planes, isotropic behavior is present since it is not possible to differentiate between directions *x* and *y*. Still, due to the application of the rotating scanning strategy, anisotropy in build direction was kept at a comparably low level; for an IN718 alloy, Serrano-Munoz et al. demonstrated that the texture index can approx. be reduced by half when a 67° rotation is applied instead of a 90° alternating *xy*-scanning scheme as a columnar grain growth with preferred < 001 > orientation over several layers is inhibited [77]. Accordingly, as stated by Safaei et al. for NiTi alloys, suppressing the grain orientation leads to a decline in anisotropy [71].

Further mechanical testing revealed differences in between bulk and LPBF material. An in situ heat treatment was assumed for the LPBF parts above. Still, the resulting microstructure did not reveal coarse and equiaxed grains as in hot-extruded parts but a finer, ten times smaller, and elongated shaping. The fact that LPBF produces a finer and non-equiaxed grain structure as present in conventional manufacturing processes has already been shown frequently in the literature for many alloy systems, including several Ni-based ones [2, 87–89]. This grain refinement in AM parts leads inevitably to a hardening of the structure, resulting in the superior mechanical properties found for yield strength and ultimate tensile strength up to 530 °C. Still, slight residual keyhole porosity was found for the additively manufactured parts by Chlupová et al., facilitating crack initiation and resulting in a more brittle material failure type than in the reference parts [90]. This gives reason for the overall lower ductility.

4.4 Reconsideration of the volume energy density as key performance indicator

As identified throughout the DoE studies, hatching of 80 μm was generally found to be unsuitable in order to reach high densities (Fig. 5). With a laser focus of approximately 50 μm, the resulting porosity can be correlated to residual lack of fusion in between scanning lines. This evidence exemplifies precisely the problem of utilizing the volume energy density as the main target figure of parameter optimizations in laser powder bed fusion processes; no matter how the residual parameters (among others, laser power, scanning speed, layer height, etc.) are adapted for a constant hatch distance, the resulting part density may not be raised to a satisfactory high value. Complete melting of the entire powder bed is not achievable for hatch distances being too broad, independently from an energy increase through, e.g., a higher laser power or a slower scanning velocity. Anyway, in modern LPBF parameter development, it is considered a general agreement to search for the optimum e_V range. Although similar volume energy densities may consist of completely different parameter combinations, this approach is widely used as applied and discussed in [48, 91, 92]. In other words, as stated in the results section, equal volume energy densities are likely to result in very different optical relative densities, which is why the e_V can only be consulted as an approximate orientation (Fig 7a). This issue has been

addressed by Scipioni Bertoli et al. in stating that e_V does not adequately describe the melt pool dynamics and must therefore be used very cautiously in LPBF parameter optimization [49]. Estrada-Díaz et al. further supported this finding by stating that the LPBF process can only be described partially with the help of VED as it lacks information on powder ejection and sublimation [93]. Single process parameters must be interpreted against the background of their interaction with other process parameters. DoE instead consists of smooth continuous parameter functions which map single parameters adequately. As the regression equation consists of the three target values of laser power, scanning speed, and hatch distance, the found parameter set fits accurately into this system. Moreover, as identified above for uncoordinated parameter sets, several kinds of defects can be found for a single layer (Fig. 8). High energy input would result in keyhole porosity, while lack of fusion and unmolten particles can be correlated with low energy introduced into the layer [51, 94]. Hence, the energy density is not distributed equally over one layer, further proof that optimum fabrication is attributable to process parameters instead of e_V. The approach of focusing on the process parameters revealed a high potential for the present Alloy 400 as high densities were achievable. While this work focused on the correlation of p_L, s_S, and d_H (input variables) with the resulting density (output variable) reduced by keyhole porosity, unmolten particles, and lack of fusion, further potential outputs such as distortion, balling, or cracking as a function of several input parameters could be investigated as well to overcome the uncoordinated nature of single process parameters. Here, applying Buckingham's π-theorem, setting the focus on the most significant physical interactions occurring, and dimensional analysis, describing a process as the sum of dimensionless products, counteract poorly adjusted parameter sets as well [95].

5 Conclusion

In this study, a holistic AM process route for Alloy 400 was established, reaching from application and alloy design according to standard specifications over in-house powder generation and characterization to a DoE-assisted laser powder bed fusion process, resulting in part microstructure analysis and comparison to conventionally fabricated material. The concrete results were then discussed and put into perspective, resulting in the following notable findings and overall conclusions of this work:

- The usable powder can be generated via the application of a close-coupled gas atomization setup using a high-temperature ceramic crucible. The final particle size distribution of 15 to 63 μm was adjusted by sieving and air-separation post-processing, resulting in spherical and

flowable particles which provided the basis for successful LPBF fabrication.

- The standard target chemical composition was in line with powders, LPBF parts, and hot-extruded reference Alloy 400, allowing us to conclude the chemical purity and consistency of the applied processes. Hence, a comparison in between the various states was enabled and carried out.

- At grain boundaries in powders, Cu segregations were clearly detectable and verified via SEM on the microscale as expected for this alloy type. Still, within printed parts, only slight micro-segregations were detected via TEM. Heat-induced diffusion processes, resulting from the iterative sequence of the LPBF process, give reason for this phenomenon as chemical imbalances may almost dissolve completely into the solid solution.

- As typical for LPBF-produced parts, a wide range of dislocations was found to be present, primarily along cell walls and occasionally inside cells. These cells were classified as micro-dendritic structures within the superordinate grains.

- The design of experiments approach for LPBF parameter development led to a final parameter set that enabled the fabrication of highly dense parts, consisting of $p_L = 85$ W, $s_S = 1050$ mm/s, $d_H = 50$ μm, and $t_L = 20$ μm, resulting in an $e_V = 80.95$ J/mm³. A rotating scanning strategy of 67° in between layers, a green laser with a wavelength of 532 nm, and a pre-heating of the build plate of 80 °C completed the parameter setup. In any case and beforehand, the basic requirement for AM material development is the identification of key parameters and resulting defect formation that prevent the production of high-density parts.

- The DoE-based approach revealed the high importance of the interdependency of single process parameters. Based on the finding that similar or even the same volume energy densities may result in very different part densities, the search for a single parameter set was found to be most expedient. Hence, for process parameter development of LPBF processes, this work greatly encourages to shift in the focus from a broad energy density range to a more integrated course of action of identifying a single optimum parameter combination. DoE does not only increase the efficiency of AM process parameter development, but the smaller number of parameter sets that need to be tested also results in overall fewer resources such as the number of build jobs, energy consumption, powder demand, and man hours.

- Mechanical properties of LPBF parts being manufactured in an upright orientation within the build space showed lower strength but higher ductility than parts being manufactured perpendicularly to the build direction. This finding was correlated with changing melt

pool formation, preferred texture, and varying anisotropy along building direction for different specimen orientations.

- At room temperature and at 530 °C, the fine-grained LPBF variant of Alloy 400 performed equally or better in terms of strength when compared to the hot-extruded, bulk reference material, revealing comparably coarse grains. At higher temperatures instead, the conventional material performed better as slight residual keyhole porosity in AM parts amplified crack initiation, compensating its beneficial microstructure.

- For elongation, the AM parts did not reach the performance of the conventional ones, which is also due to porosity acting as a fracture trigger and causing a more brittle failure mode. Moreover, this is connected to the inverted relationship between strength (which is higher in AM parts) and elongation.

- The hardness of LPBF-built parts was significantly higher compared to conventionally fabricated material being correlated to the coarser grain size of the hot-extruded material.

Declarations

Competing Interests The authors declare no competing interests.

References

1. Special Metals Corporation (2005) Monel Alloy 400. https://www.specialmetals.com/documents/technical-bulletins/monel-alloy-400.pdf

2. Raffeis I, Adjei-Kyeremeh F, Vroomen U et al (2020) Qualification of a Ni–Cu alloy for the laser powder bed fusion process (LPBF): its microstructure and mechanical properties. Appl Sci 10:3401. https://doi.org/10.3390/app10103401

3. Zhang C-H, Wu C-L, Zhang S et al (2022) Laser cladding of NiCrSiB on Monel 400 to enhance cavitation erosion and corrosion resistance. Rare Met 41:4257–4265. https://doi.org/10.1007/s12598-016-0814-4

4. Esgin U, Özyürek D, Kaya H (2016) An investigation of wear behaviors of different Monel alloys produced by powder metallurgy. AIP Conf Proc 1727:20008. https://doi.org/10.1063/1.4945963

5. Kukliński M, Bartkowska A, Przestacki D (2018) Microstructure and selected properties of Monel 400 alloy after laser heat treatment and laser boriding using diode laser. Int J Adv Manuf Technol 98:3005–3017. https://doi.org/10.1007/s00170-018-2343-9

6. Devendranath RK, Arivazhagan N, Narayanan S et al (2011) Development of defect free Monel 400 welds for marine application. AMR 383–390:4693–4696. https://doi.org/10.4028/www.scientific.net/AMR.383-390.4693

7. Special Metals Corporation (2000) High-performance alloys for resistance to aqueous corrosion. https://www.specialmetals.com/documents/aqueous-corrosion-handbook.pdf

8. Shoemaker LE, Smith GD (2006) A century of Monel metal: 1906–2006. JOM 58:22–26. https://doi.org/10.1007/s11837-006-0077-x

9. Zils R (2008) Werkstoffe im Pumpenbau. Chem Ing Tec 80:499–508. https://doi.org/10.1002/cite.200700183

10. Ventrella VA, Berretta JR, de Rossi W (2011) Micro welding of Ni-based alloy Monel 400 thin foil by pulsed Nd:YAG laser. Phys Procedia 12:347–354. https://doi.org/10.1016/j.phpro.2011.03.143

11. Maier HJ, Niendorf T, Bürgel R (2019) Handbuch Hochtemperatur-Werkstofftechnik. Springer Vieweg, Wiesbaden

12. Bargel H-J (2022) Werkstoffkunde. Springer, Berlin Heidelberg, Berlin, Heidelberg

13. Young DJ, Zhang J, Geers C et al (2011) Recent advances in understanding metal dusting: a review. Mater Corros 62:7–28. https://doi.org/10.1002/maco.201005675

14. Schneider R, Pippel E, Woltersdorf J et al (1997) Micropro-cesses of metal dusting on nickel and Ni-base alloys. Steel Research 68:326–332. https://doi.org/10.1002/srin.199701796

15. Jahns K, Ulrich AS, Schlereth C et al (2021) The effect of Cu content and surface finish on the metal dusting resistance of additively manufactured NiCu alloys. Oxid Met 96:241–256. https://doi.org/10.1007/s11085-021-10037-8

16. Abdulhameed O, Al-Ahmari A, Ameen W et al (2019) Additive manufacturing: challenges, trends, and applications. Adv Mech Eng 11:168781401882288. https://doi.org/10.1177/1687814018822880

17. Ramazani H, Kami A (2022) Metal FDM, a new extrusion-based additive manufacturing technology for manufacturing of metal-lic parts: a review. Prog Addit Manuf 7:609–626. https://doi.org/10.1007/s40964-021-00250-x

18. Yap CY, Chua CK, Dong ZL et al (2015) Review of selec-tive laser melting: materials and applications. Appl Phys Rev 2:41101. https://doi.org/10.1063/1.4935926

19. Popovich A, Sufiiarov V (2016) Metal powder additive manufac-turing. New Trends in 3D Printing. https://doi.org/10.5772/63337

20. Dunkley JJ (2019) Metal powder atomisation methods for mod-ern manufacturing. Johnson Matthey Technol Rev 63:226–232. https://doi.org/10.1595/205651319X15583434137356

21. Antony LVM, Reddy RG (2003) Processes for production of high-purity metal powders. JOM 55:14–18. https://doi.org/10.1007/s11837-003-0153-4

22. Hussain S, Cui C, He L et al (2020) Effect of hot gas atomi-zation on spray forming of steel tubes using a close-coupled atomizer (CCA). J Mater Process Technol 282:116677. https://doi.org/10.1016/j.jmatprotec.2020.116677

23. Mathews PG (2005) Design of experiments with MINITAB. ASQ Quality Press, Milwaukee, WI, USA

24. Czitrom V (1999) One-factor-at-a-time versus designed experi-ments. Am Stat 53:126–131. https://doi.org/10.1080/00031305.1999.10474445

25. Tanco M, Viles E, Pozueta L (2008) Are all designs of experi-ments approaches suitable for your Company? Proceedings of the World Congress on Engineering 2008, Vol. 2 WCE. London

26. Tanco M, Viles E, Ilzarbe L et al. (2007) Manufacturing indus-tries need design of experiments (DoE). Proceedings of the World Congress on Engineering 2007, Vol. 2 WCE. London

27. Cavazzuti M (2013) Design of experiments. In: Cavazzuti M (ed) Optimization methods. Springer, Berlin Heidelberg, Berlin, Heidelberg, pp 13–42

28. Bourell D, Kruth JP, Leu M et al (2017) Materials for addi-tive manufacturing. CIRP Ann 66:659–681. https://doi.org/10.1016/j.cirp.2017.05.009

29. Clare AT, Reynolds WJ, Murray JW et al (2020) Laser calorim-etry for assessment of melting behaviour in multi-walled car-bon nanotube decorated aluminium by laser powder bed fusion. CIRP Ann 69:197–200. https://doi.org/10.1016/j.cirp.2020.04.053

30. Schwenck D, Ellendt N, Fischer-Bühner J et al (2017) A novel convergent–divergent annular nozzle design for close-coupled atomisation. Powder Metall 60:198–207. https://doi.org/10.1080/00325899.2017.1291098

31. Mullis AM, Farrell L, Cochrane RF et al (2013) Estimation of cooling rates during close-coupled gas atomization using second-ary dendrite arm spacing measurement. Metall Mater Trans B 44:992–999. https://doi.org/10.1007/s11663-013-9856-2

32. Ciftci N, Ellendt N, Coulthard G et al (2019) Novel cooling rate correlations in molten metal gas atomization. Metall Mater Trans B 50:666–677. https://doi.org/10.1007/s11663-019-01508-0

33. Soares Barreto E, Frey M, Wegner J et al (2022) Properties of gas-atomized Cu-Ti-based metallic glass powders for additive manufacturing. Mater Des 215:110519. https://doi.org/10.1016/j.matdes.2022.110519

34. Blue Power Casting and Powder Production Systems (2023) AUG-Series catalogue. https://bluepower-casting.com/media/e4/47/38/1674564361/Indutherm_Catalogue_en_2023_web_DS.pdf

35. Sun P, Fang ZZ, Zhang Y et al (2017) Review of the methods for production of spherical Ti and Ti alloy powder. JOM 69:1853–1860. https://doi.org/10.1007/s11837-017-2513-5

36. Cohn R, Anderson I, Prost T et al (2021) Instance segmentation for direct measurements of satellites in metal powders and auto-mated microstructural characterization from image data. JOM 73:2159–2172. https://doi.org/10.1007/s11837-021-04713-y

37. Erdélyi Z, Girardeaux C, Tôkei Z et al (2002) Investigation of the interplay of nickel dissolution and copper segregation in Ni/Cu(111) system. Surf Sci 496:129–140. https://doi.org/10.1016/S0039-6028(01)01571-0

38. Pellicer E, Varea A, Sivaraman KM et al (2011) Grain boundary segregation and interdiffusion effects in nickel-copper alloys: an effective means to improve the thermal stability of nanocrystalline nickel. ACS Appl Mater Interfaces 3:2265–2274. https://doi.org/10.1021/am2004587

39. Naghash AR, Etsell TH, Xu S (2006) XRD and XPS study of Cu−Ni interactions on reduced copper−nickel−aluminum oxide solid solution catalysts. Chem Mater 18:2480–2488. https://doi.org/10.1021/cm051910o

40. Kearns M (2004) Development and applications of ultrafine alu-minium powders. Mater Sci Eng, A 375–377:120–126. https://doi.org/10.1016/j.msea.2003.10.160

41. Slotwinski JA, Garboczi EJ, Stutzman PE et al (2014) Characteri-zation of metal powders used for additive manufacturing. J Res Natl Inst Stand Technol 119:460–493. https://doi.org/10.6028/jres.119.018

42. Sun J, Guo M, Shi K et al (2022) Influence of powder morphol-ogy on laser absorption behavior and printability of nanoparticle-coated 90W-Ni-Fe powder during laser powder bed fusion. Mater Sci Add Manuf 1. https://doi.org/10.18063/msam.v1i2.11

43. Sendino S, Martinez S, Lamikiz A (2020) Characterization of IN718 recycling powder and its effect on LPBF manufactured parts. Procedia CIRP 94:227–232. https://doi.org/10.1016/j.procir.2020.09.043

44. Zegzulka J, Gelnar D, Jezerska L et al (2020) Characterization and flowability methods for metal powders. Sci Rep 10:21004. https://doi.org/10.1038/s41598-020-77974-3

45. Saw HY, Davies CE, Paterson AH et al (2015) Correlation between powder flow properties measured by shear testing and Hausner ratio. Procedia Eng 102:218–225. https://doi.org/10.1016/j.proeng.2015.01.132

46. Abdullah EC, Geldart D (1999) The use of bulk density measure-ments as flowability indicators. Powder Technol 102:151–165. https://doi.org/10.1016/s0032-5910(98)00208-3

47. Hao T (2015) Understanding empirical powder flowability criteria scaled by Hausner ratio or Carr index with the analogous viscos-ity concept. RSC Adv 5:57212–57215. https://doi.org/10.1039/C5RA07197F

48. Ciurana J, Hernandez L, Delgado J (2013) Energy density analysis on single tracks formed by selective laser melting with CoCrMo powder material. Int J Adv Manuf Technol 68:1103–1110. https://doi.org/10.1007/s00170-013-4902-4

49. Scipioni Bertoli U, Wolfer AJ, Matthews MJ et al (2017) On the limitations of volumetric energy density as a design parameter for selective laser melting. Mater Des 113:331–340. https://doi.org/10.1016/j.matdes.2016.10.037

50. Kasperovich G, Haubrich J, Gussone J et al (2016) Correlation between porosity and processing parameters in TiAl6V4 produced by selective laser melting. Mater Des 105:160–170. https://doi.org/10.1016/j.matdes.2016.05.070

51. Shrestha S, Starr T, Chou K (2019) A study of keyhole porosity in selective laser melting: single-track scanning with micro-CT analysis. J Manuf Sci Eng 141. https://doi.org/10.1115/1.4043622

52. Gan Z, Kafka OL, Parab N et al (2021) Universal scaling laws of keyhole stability and porosity in 3D printing of metals. Nat Commun 12:2379. https://doi.org/10.1038/s41467-021-22704-0

53. Yu SJ, Wang P, Li HC et al (2023) Heterogeneous microstructure and mechanical behaviour of Al-8.3Fe-1.3V-1.8Si alloy produced by laser powder bed fusion. Virtual Phys Prototyp 18:e2155197. https://doi.org/10.1080/17452759.2022.2155197

54. Krakhmalev P, Fredriksson G, Svensson K et al (2018) Microstructure, solidification texture, and thermal stability of 316 L stainless steel manufactured by laser powder bed fusion. Metals 8:643. https://doi.org/10.3390/met8080643

55. Qin H, Fallah V, Dong Q et al (2018) Solidification pattern, microstructure and texture development in laser powder bed fusion (LPBF) of Al10SiMg alloy. Mater Charact 145:29–38. https://doi.org/10.1016/j.matchar.2018.08.025

56. Zhang XX, Andrä H, Harjo S et al (2021) Quantifying internal strains, stresses, and dislocation density in additively manufactured AlSi10Mg during loading-unloading-reloading deformation. Mater Des 198:109339. https://doi.org/10.1016/j.matdes.2020.109339

57. Martin N, Hor A, Copin E et al (2022) Correlation between microstructure heterogeneity and multi-scale mechanical behavior of hybrid LPBF-DED Inconel 625. J Mater Process Technol 303:117542. https://doi.org/10.1016/j.jmatprotec.2022.117542

58. Voisin T, Forien J-B, Perron A et al (2021) New insights on cellular structures strengthening mechanisms and thermal stability of an austenitic stainless steel fabricated by laser powder-bed-fusion. Acta Mater 203:116476. https://doi.org/10.1016/j.actamat.2020.11.018

59. Sabzi HE, Hernandez-Nava E, Li X-H et al (2021) Strengthening control in laser powder bed fusion of austenitic stainless steels via grain boundary engineering. Mater Des 212:110246. https://doi.org/10.1016/j.matdes.2021.110246

60. Kong D, Dong C, Wei S et al (2021) About metastable cellular structure in additively manufactured austenitic stainless steels. Addit Manuf 38:101804. https://doi.org/10.1016/j.addma.2020.101804

61. Li Z, He B, Guo Q (2020) Strengthening and hardening mechanisms of additively manufactured stainless steels: the role of cell sizes. Scripta Mater 177:17–21. https://doi.org/10.1016/j.scriptamat.2019.10.005

62. Wang YM, Voisin T, McKeown JT et al (2018) Additively manufactured hierarchical stainless steels with high strength and ductility. Nat Mater 17:63–71. https://doi.org/10.1038/nmat5021

63. Gruber K, Smolina I, Kasprowicz M et al (2021) Evaluation of Inconel 718 metallic powder to optimize the reuse of powder and to improve the performance and sustainability of the laser powder bed fusion (LPBF) process. Materials 14:1538. https://doi.org/10.3390/ma14061538

64. Ardila LC, Garciandia F, González-Díaz JB et al (2014) Effect of IN718 recycled powder reuse on properties of parts manufactured by means of selective laser melting. Phys Procedia 56:99–107. https://doi.org/10.1016/j.phpro.2014.08.152

65. Field AC, Carter LN, Adkins NJE et al (2020) The effect of powder characteristics on build quality of high-purity tungsten produced via laser powder bed fusion (LPBF). Metall Mater Trans A 51:1367–1378. https://doi.org/10.1007/s11661-019-05601-6

66. Estrada-Díaz JA, Elías-Zúñiga A, Martínez-Romero O et al (2024) A novel mathematical model for predicting a sustainable selective laser melting and controlled densification. Int J Sustain Eng 17:1–11. https://doi.org/10.1080/19397038.2024.2327386

67. ESTRADA-DÍAZ JA, MARTÍNEZ-ROMERO O, OLVERA-TREJO D et al (2022) Elucidating the fractal nature of powder bed in selective laser melting of metallic components. Fractals 30. https://doi.org/10.1142/S0218348X22500621

68. Jodi DE, Kitashima T, Singh A et al (2023) High-temperature microstructural stability of pure Ni fabricated by laser powder bed fusion using Gaussian and flat-top beam profiles. Mater Charact 200:112897. https://doi.org/10.1016/j.matchar.2023.112897

69. Suwas S, Ray RK (2014) Crystallographic texture of materials. Engineering Materials and Processes, Springer London, London

70. Dantzig JS, Rappaz M (2016) Solidification methods microstructure and modelling. CRC Press, Boca Raton, Engineering sciences Materials

71. Safaei K, Abedi H, Nematollahi M et al (2021) Additive manufacturing of NiTi shape memory alloy for biomedical applications: review of the LPBF process ecosystem. JOM 73:3771–3786. https://doi.org/10.1007/s11837-021-04937-y

72. Pilz S, Gustmann T, Günther F et al (2022) Controlling the Young's modulus of a ß-type Ti-Nb alloy via strong texturing by LPBF. Mater Des 216:110516. https://doi.org/10.1016/j.matdes.2022.110516

73. Hooper PA (2018) Melt pool temperature and cooling rates in laser powder bed fusion. Addit Manuf 22:548–559. https://doi.org/10.1016/j.addma.2018.05.032

74. Qin H, Dong Q, Fallah V et al (2020) Rapid solidification and non-equilibrium phase constitution in laser powder bed fusion (LPBF) of AlSi10Mg alloy: analysis of nano-precipitates, eutectic phases, and hardness evolution. Metall Mater Trans A 51:448–466. https://doi.org/10.1007/s11661-019-05505-5

75. He Y, Zhong M, Jones N et al (2021) The columnar-to-equiaxed transition in melt pools during laser powder bed fusion of M2 steel. Metall Mater Trans A 52:4206–4221. https://doi.org/10.1007/s11661-021-06380-9

76. Pant P, Salvemini F, Proper S et al (2022) A study of the influence of novel scan strategies on residual stress and microstructure of L-shaped LPBF IN718 samples. Mater Des 214:110386. https://doi.org/10.1016/j.matdes.2022.110386

77. Serrano-Munoz I, Ulbricht A, Fritsch T et al (2021) Scanning manufacturing parameters determining the residual stress state in LPBF IN718 small parts. Adv Eng Mater 23:2100158. https://doi.org/10.1002/adem.202100158

78. Solheid JS, Elkaseer A, Wunsch T et al (2022) Multiobjective optimization of laser polishing of additively manufactured Ti-6Al-4V parts for minimum surface roughness and heat-affected zone. Materials 15:3323. https://doi.org/10.3390/ma15093323

79. Hatakeyama T, Sawada K, Suzuki M et al (2023) Microstructure development of modified 9Cr-1Mo steel during laser powder bed fusion and heat treatment. Addit Manuf 61:103350. https://doi.org/10.1016/j.addma.2022.103350

80. Bertsch KM, Meric de Bellefon G, Kuehl B et al (2020) Origin of dislocation structures in an additively manufactured austenitic stainless steel 316L. Acta Mater 199:19–33. https://doi.org/10.1016/j.actamat.2020.07.063

81. Bassini E, Sivo A, Martelli PA et al (2022) Effects of the solution and first aging treatment applied to as-built and post-HIP CM247 produced via laser powder bed fusion (LPBF). J Alloy Compd 905:164213. https://doi.org/10.1016/j.jallcom.2022.164213

82. Cox B, Ghayoor M, Doyle RP et al (2022) Numerical model of heat transfer during laser powder bed fusion of 316L stainless steel. Int J Adv Manuf Technol 119:5715–5725. https://doi.org/10.1007/s00170-021-08352-0

83. Wilson-Heid AE, Wang Z, McCornac B et al (2017) Quantitative relationship between anisotropic strain to failure and grain morphology in additively manufactured Ti-6Al-4V. Mater Sci Eng, A 706:287–294. https://doi.org/10.1016/j.msea.2017.09.017

84. Yu C-H, Peng RL, Lee TL et al (2022) Anisotropic behaviours of LPBF Hastelloy X under slow strain rate tensile testing at elevated

temperature. Mater Sci Eng, A 844:143174. https://doi.org/10.1016/j.msea.2022.143174

85. Pérez-Ruiz JD, Marin F, Martínez S et al (2022) Stiffening near-net-shape functional parts of Inconel 718 LPBF considering material anisotropy and subsequent machining issues. Mech Syst Signal Process 168:108675. https://doi.org/10.1016/j.ymssp.2021.108675

86. Fedorenko A, Fedulov B, Kuzminova Y et al (2021) Anisotropy of mechanical properties and residual stress in additively manufactured 316L specimens. Materials 14:7176. https://doi.org/10.3390/ma14237176

87. Avateffazeli M, Carrion PE, Shachi-Amirkhiz B et al (2022) Correlation between tensile properties, microstructure, and processing routes of an Al–Cu–Mg–Ag–TiB2 (A205) alloy: additive manufacturing and casting. Mater Sci Eng, A 841:142989. https://doi.org/10.1016/j.msea.2022.142989

88. Li C, White R, Fang XY et al (2017) Microstructure evolution characteristics of Inconel 625 alloy from selective laser melting to heat treatment. Mater Sci Eng, A 705:20–31. https://doi.org/10.1016/j.msea.2017.08.058

89. Raghavan S, Zhang B, Wang P et al (2017) Effect of different heat treatments on the microstructure and mechanical properties in selective laser melted Inconel 718 alloy. Mater Manuf Processes 32:1588–1595. https://doi.org/10.1080/10426914.2016.1257805

90. Chlupová A, Šulák I, Kuběna I et al (2023) Comparison of microstructure and properties of nickel-copper alloy prepared by casting and laser powder bed fusion process. MSF 1082:171–176. https://doi.org/10.4028/p-884q32

91. Ghayoor M, Lee K, He Y et al (2020) Selective laser melting of 304L stainless steel: role of volumetric energy density on the microstructure, texture and mechanical properties. Addit Manuf 32:101011. https://doi.org/10.1016/j.addma.2019.101011

92. Megahed S, Aniko V, Schleifenbaum JH (2022) Electron beam-melting and laser powder bed fusion of Ti6Al4V: transferability of process parameters. Metals 12:1332. https://doi.org/10.3390/met12081332

93. Estrada-Díaz JA, Elías-Zúñiga A, Martínez-Romero O et al (2021) A mathematical dimensional model for predicting bulk density of Inconel 718 parts produced by selective laser melting. Materials 14:512. https://doi.org/10.3390/ma14030512

94. de Terris T, Andreau O, Peyre P et al (2019) Optimization and comparison of porosity rate measurement methods of selective laser melted metallic parts. Addit Manuf 28:802–813. https://doi.org/10.1016/j.addma.2019.05.035

95. Estrada-Díaz JA, Elías-Zúñiga A, Martínez-Romero O et al (2021) Enhanced mathematical model for producing highly dense metallic components through selective laser melting. Materials 14:1571. https://doi.org/10.3390/ma14061571

Publisher's Note Springer Nature remains neutral with regard to jurisdictional claims in published maps and institutional affiliations.